Enhancement of electrochemical performance of SrFe$_{0.5}$Co$_{0.5}$O$_{3-\delta}$ as air electrode for intermediate temperature solid oxide cells via Sb and Mo doping

Víctor Zapata-Ramírez, Glenn C. Mather, Domingo Pérez-Coll [*]

Instituto de Cerámica y Vidrio (ICV), CSIC, C/Kelsen, 5, 28049, Madrid, Spain

ABSTRACT

Optimisation of the composition or rare-earth-free perovskites is of considerable interest for their application as air electrodes in intermediate temperature solid oxide cells (IT-SOCs). Herein, we report the effects of Mo and Sb doping (5 mol %) of SrFe$_{0.5}$Co$_{0.5}$O$_{3-\delta}$ (SFC) on oxygen content, thermal behaviour, electrochemical properties and stability. Phase-pure, XRD-cubic perovskite is achieved on sintering powder derived from Pechini synthesis in the range 1000–1100 °C for SFC, SrFe$_{0.475}$Co$_{0.475}$Mo$_{0.05}$O$_{3-\delta}$ (SFCM) and SrFe$_{0.475}$Co$_{0.475}$Sb$_{0.05}$O$_{3-\delta}$ (SFCSb). Oxygen content determined by redox titration is greater for the Mo- and Sb-doped phases than for SFC, although oxygen loss occurring at > 350 °C is greatest for SFCSb. The higher total oxygen content of the Mo-doped phase is expected to increase the electron-hole content resulting in higher conductivity (σ = 340.5 S cm^{-1} at 300 °C in O$_2$). In contrast, the greater oxygen-vacancy content with increasing temperature of the Sb-doped material is associated with the most competitive electrode-polarisation resistance (<0.1 Ω cm^2 at 700 °C). The greater relative effect of cathodic and anodic polarisation on improving electrochemical performance at lower temperatures highlights the potential of the studied compositions as air electrodes in IT-SOCs.

1. Introduction

Solid oxide fuel cells (SOFCs) are highly efficient and versatile high-temperature fuel-to-power conversion devices [1,2], which are very attractive for application with combined technologies such as gas turbines and high-technology solar devices [3–5]. SOFCs operating on hydrogen are particularly promising for the transition to clean and green electricity production in the endeavour to limit greenhouse-gas emissions and pollution. A further advantage of these electrochemical cells is their reversibility, on operation as electrolysers (solid oxide electrolysis cell, SOEC) providing hydrogen from water and low-carbon fuels from CO$_2$ [6–10]. Their principal disadvantage is the high working temperature, 800 – 1000 °C, which causes degradation and incompatibility issues between the ceramic components. Hence, a major goal is lowering the working temperature to the intermediate-temperature range (550 – 800 °C) while concomitantly maintaining high efficiency and the potential reversibility of the system (IT-RSOC, intermediate temperature reversible solid oxide cell) [11–13].

The selection of the air electrode is particularly critical as polarisation resistance is especially affected by the reduction of the working temperature [14–16]. Innovative materials for air electrodes include ceramic oxides with good mixed ionic-electronic conductivity in oxidising atmospheres, such as some families of perovskites (ABO$_{3-\delta}$), which enjoy ease of synthesis and adaptability of their properties through composition selection and doping [17]. Strontium-doped lanthanum manganite (La$_{1-x}$Sr$_x$MnO$_{3-\delta}$, LSM) has traditionally been targeted for temperatures above 850 °C due to its high physicochemical stability with yttrium-stabilised zirconia (YSZ) electrolyte. However, LSM exhibits rather poor electrochemical properties attributable to low ionic conductivity [16,18]. Partial or complete substitution of Mn for Co or Fe on the B site of LSM (Ln$_{1-x}$Sr$_x$Co$_{1-y}$Mn$_y$O$_{3-\delta}$, Ln$_{1-x}$Sr$_x$Co$_{1-y}$Fe$_y$O$_{3-\delta}$, where Ln is a lanthanide) favours electrochemical performance although stability is generally poorer [19]. Some of the most studied groups of perovskite materials for air electrodes in solid oxide cells, especially intermediate-temperature operation, include cobaltites, ferrites and cobaltite-ferrites, due to their high mixed oxide-ionic and electronic conductivities [16]. Systems which incorporate lanthanides (principally La, Gd, Sm, Nd and Pr) and alkaline-earths (mainly Ba, Sr and Ca) in the A position of the perovskite are commonly studied due to their high oxygen-vacancy concentrations and mixed oxidation states of the

---

* Corresponding author.
  E-mail address: dpcoll@icv.csic.es (D. Pérez-Coll).

transition-metal cations [15].

However, rare-earth elements are in much demand with crucial roles in many technological applications, increasing their cost [20–22]. Moreover, their location in geopolitically sensitive countries has a further negative effect on rare-earth prices. Hence, lowering production costs by decreasing the lanthanide content in air-electrode compositions will be a necessary strategy for widespread implementation of solid oxide cells.

For operation in the intermediate temperature range, highly performing air electrodes have been obtained with the $SrCoO_{3-\delta}$ (SCO) family doped on the Co site. The pristine composition is characterised by a phase transition from cubic to hexagonal symmetry on decreasing the temperature below 900 °C; however, the lower symmetry phase is associated with both a drastically reduced electrical conductivity and electrochemical performance [24]. The introduction of suitable cations in the B position, such as Nb [23], Sb [24], Ta [25], Sc [26] and Mo [27], stabilises the cubic phase at room temperature, improving the electrochemical efficiency. Nevertheless, the excessive presence of Co causes stability problems, which is considerably improved on partial substitution of the B-site cation with a higher-valence dopant [28,29]. As is the case for rare earths, cobalt is also a critical resource, with high demand in technological applications, particularly for lithium-ion batteries [30]; it is also associated with socioeconomic issues related to its principal mining source in the Democratic Republic of the Congo [31]. Consequently, lowering the Co content in SCO-based families on partial or complete substitution for Fe and high-valence cations is the focus of much SOFC cathode research [23–25,27,29,32–36].

The aim of the present work is the preparation of air-electrode materials based on the SCO parent phase which are both free of rare-earth elements and are of lower Co content. Specifically, the effects of Mo and Sb doping are studied in detail for the phase $SrFe_{0.5}Co_{0.5}O_{3-\delta}$ at a doping level of 5 at.% ($SrFe_{0.475}Co_{0.475}Mo_{0.05}O_{3-\delta}$ and $SrFe_{0.475}Co_{0.475}Sb_{0.05}O_{3-\delta}$) and compared to $SrFe_{0.5}Co_{0.5}O_{3-\delta}$ in an endeavour to optimise electrochemical performance and stability in air electrodes consisting of more sustainable elements.

2. Experimental

2.1. Synthesis, structure and microstructure

Pechini synthesis [37] was employed to obtain $SrFe_{0.5}Co_{0.5}O_{3-\delta}$ (SFC), $SrFe_{0.475}Co_{0.475}Mo_{0.05}O_{3-\delta}$ (SFCM) and $SrFe_{0.475}Co_{0.475}Sb_{0.05}O_{3-\delta}$ (SFCSb). Stoichiometric amounts of $Sr(NO_3)_2$, $Fe(NO_3)_3 \cdot 6H_2O$, $Co(NO_3)_2 \cdot 6H_2O$, $(NH_4)_6Mo_7O_{24} \cdot 4H_2O$, and Sb_2O_3 were dissolved in deionised water with continuous stirring on a hotplate at 50 °C; dissolution of Sb_2O_3 was achieved on addition of drops of HNO_3. Subsequently, citric acid and ethylene glycol were added as chelating and complexing agents in molar ratios of 10:1 and 40:1 regarding the total moles of product, respectively. Polycondensation occurred on increasing the temperature to 100 °C overnight, producing a dark and viscous mass. Subsequently, the samples underwent heat treatment at 350 and 600 °C, followed by grinding in an agate mortar. Final firing was performed in the range 1000 – 1100 °C to achieve phase purity, prior to milling (400 rpm for 2 h in a Fritsch pulverisette planetary ball mill) and sieving to a fine powder.

Structural characterisation was performed using X-ray diffraction (XRD) data collected in the range $20° \leq 2\theta \leq 70°$ with a stepwidth of 0.02° on a Bruker D8 high-resolution diffractometer equipped with a Ge monochromator providing monochromatic $CuK\alpha_1$ radiation ($\lambda = 1.5406$ Å) at 40 kV and 40 mA. Rietveld refinement was performed with the Fullprof software [38]. The microstructure and morphology of

electrode-electrolyte half-cells sputtered with a thin gold coating was examined by scanning electron microscopy (SEM) with a FE-SEM Hitachi 4700 S microscope.

2.2. Oxygen content, oxidation states and thermal analysis

Redox titration was carried out to determine the oxygen content and the oxidation states of the cations in the samples at room temperature, as reported previously [39–41] and described as follows. Different amounts of Mohr's salt and powders of the studied crystalline phases were dissolved in a volumetric flask on addition of milliQ water, HCl, H_3PO_4 and the indicator ferroine ($(C_{36}H_{24}FeN_6)SO_4$). Argon was continuously bubbled through the solution to avoid the oxidising effect of the air atmosphere. The end point was detected by the change of colour of the solution from red to green.

Thermogravimetry was performed in air using a TGA Setsys evolution equipment using powders of synthesised phases in the range RT-900 °C with a heating/cooling rate of 10 °C·min^{-1}. For dilatometry, sintered bars ($12 \times 4 \times 4$ mm^3) with relative densifications ~ 92-94% were prepared by pressing powders at 100 MPa and firing at 1200 °C for 6 h. Linear-thermal expansion analysis was performed in the range RT – 900 °C using a Netzsch DIL 402 PC instrument.

2.3. Electrical conductivity

Dense bars, obtained in a similar manner to those used in dilatometry, were used to study the electrical conductivity by a 4-probe methodology on attaching one pair of platinum wires to the external Pt-covered surfaces, for electrical current flow, and another pair was internally attached to read the voltage. Pt paint (Heraeus) was used to connect Pt wires to the bars and cover the external rectangular surfaces, prior to firing the bars at 950 °C for 1h to ensure good contact. A Metrohm Autolab PGSTAT302 N potentiostat/galvanostat with GPES software was employed to collect I-V curves on applying direct current in galvanostatic mode in the range 0 - 100 mA. The measurements were performed under steady-state conditions in flowing air, oxygen and nitrogen atmospheres at a rate of 50 ml/min on cooling in the range 150 - 900 °C, with intervals of 50 °C and with heating/cooling rates of 5 °C/min.

2.4. Electrochemical analysis

Electrode-electrolyte half-cells were analysed by impedance spectroscopy to study the electrode polarisation resistance. $Co(NO_3)_2 \cdot 6H_2O$ (2 mol %) was added as sintering agent to $Ce_{0.9}Gd_{0.1}O_{2-\delta}$ (CGO) electrolyte powder (Rhodia) and the mixture heat treated at 650 °C for 1h [42]. The powder was subsequently uniaxially pressed and sintered at 1100 °C for 6h to obtain disks of ~1 mm thickness and ~15 mm diameter. The electrode under study was mixed with a commercial liquid organic agent (Decoflux) to form an ink and brushed on both sides of the electrolyte through a mask of diameter 6 mm. The electrode-electrolyte assemblies were then fired at 1000 °C for 2h. For 3-probe electrode polarisation measurements, a reference Pt electrode was attached to the outer circumference of one side of the electrolyte membrane using Pt paint and wire [43]. Impedance spectroscopy was performed with a Metrohm Autolab PGSTAT302 N, applying a potential amplitude of 50 mV in a frequency range of 0.1 - 10^6 Hz and temperature range of 600 - 900 °C. The effect of current on the electrochemical performance was evaluated by impedance spectroscopy in the same frequency range with a signal amplitude of 1 mA and simultaneous direct currents between 0 and 400 mA cm^{-2}, under both cathodic and

anodic polarisation. The analysis of impedance spectra and corresponding equivalent circuit fitting were performed by means of the Zview software (Scribner Associates).

2.5. Stability

Electrochemical stability of the half cells was evaluated both on performing impedance spectroscopy at 700 °C for 100 h, in steps of 3 h, and on cycling the temperature (10 heating-cooling cycles) between 300 and 800 °C.

3. Results

3.1. Structural and microstructural characterisation

Room temperature XRD patterns of SFC and SFCM with final firing temperature of 1000 °C, and SFCSb with firing temperature of 1100 °C, are shown in Fig. 1. At the resolution of XRD, single-phase perovskite with cubic symmetry (space group $Pm\bar{3}m$) is confirmed for the three samples. These results agree well with previous reports confirming that the $SrFe_{1-x}Co_xO_{3-\delta}$ family adopts tetragonal symmetry for $0 \leq x \leq 0.2$ [44,45] and cubic symmetry for $0.3 \leq x \leq 0.7$ [45,46]. Mo and Sb are also effective dopants for stabilisation of the cubic phase in both $SrCoO_{3-\delta}$ and $SrFeO_{3-\delta}$ systems [24,27,44,47,48]. Combination of Fe-Co-Sb/Mo on the B-site of the perovskite employed in the current work retains cubic symmetry at low temperature. Substituting the B site of the perovskite with 5% Mo reduces the lattice parameter from a = 3.8675(2) Å (corresponding to SFC) to 3.8612(2) Å, whereas it increases on introduction of Sb to a = 3.8740(5) Å.

The lattice parameters of all samples are in the expected range for similar compositions, e.g. 3.866 Å for $SrFe_{0.6}Co_{0.4}O_{3-\delta}$ [46], 3.865 Å for $SrFe_{0.5}Co_{0.5}O_{3-\delta}$ [45], 3.864 Å for $SrFe_{0.4}Co_{0.6}O_{3-\delta}$ [49] or 3.869 Å for $SrFe_{0.45}Co_{0.45}Mo_{0.1}O_{3-\delta}$ [50].

It should be mentioned that comparison between results from different literature sources should be performed with care, given that the lattice parameters are influenced, not only by the respective content of cations, but also by their oxidation states, which are dependent on preparation route, thermal treatment and thermal history. In the current work, the modification of the dimensions of the unit cell on doping correlate very well with the relations between the ionic radii of the dopants and the contents of respectively larger and smaller 3+ and 4+ host species, as will be discussed later.

Scanning electron micrographs (Fig. 2) reveal homogenous samples free of secondary phases after deposition and sintering at 1000 °C. Although the three compositions present a similar morphology, a slightly larger grain size is inferred for SFCSb as a consequence of its higher firing temperature. All samples show good porosity and improved intergranular connectivity compared to similar $SrFeO_{3-\delta}$-based materials obtained by the same synthesis method [44,51], which is expected to enhance oxygen diffusion across the electrode surface for the oxygen-reduction and oxidation reactions in each case. The samples present good adhesion between the electrode and the electrolyte, without apparent cracks or delamination. A homogeneous air-electrode thickness of ~30-40 μm was obtained for the different compositions.

3.2. Oxygen content, oxidation states and thermal analysis

The average oxidation state of (Fe,Co) and the oxygen content at room temperature for the three studied materials are collected in Table 1. We note that the oxidation state of molybdenum and antimony were considered as +6 and +5, respectively, as is typically assumed for similar systems [24,27,47,48,50,52,53]. In this regard, it was previously reported that molybdenum species reside as Mo^{6+} in the $Sr_2Fe_{2-x}Mo_xO_{6-\delta}$ system under air, limiting the molybdenum solubility, and that the only way to increase solubility and produce Mo^{5+} species is by decreasing the
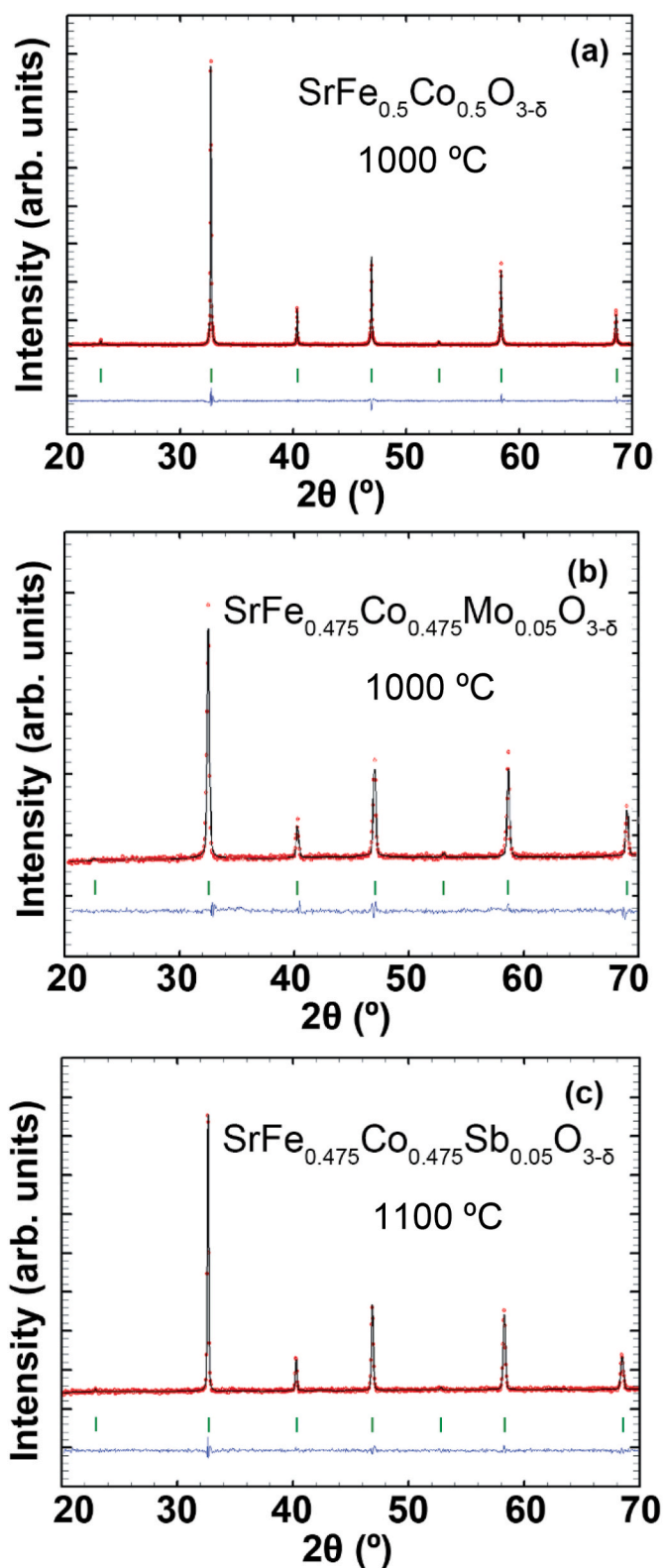

Fig. 1. Experimental (red circles), calculated (continuous black line) and difference (continuous blue line at bottom of each panel) XRD patterns of (a) $SrFe_{0.5}Co_{0.5}O_{3-\delta}$, (b) $SrFe_{0.475}Co_{0.475}Mo_{0.05}O_{3-\delta}$ and (c) $SrFe_{0.475}Co_{0.475}Sb_{0.05}O_{3-\delta}$. The positions of Bragg peaks are indicated by vertical bars. (For interpretation of the references to colour in this figure legend, the reader is referred to the Web version of this article.)
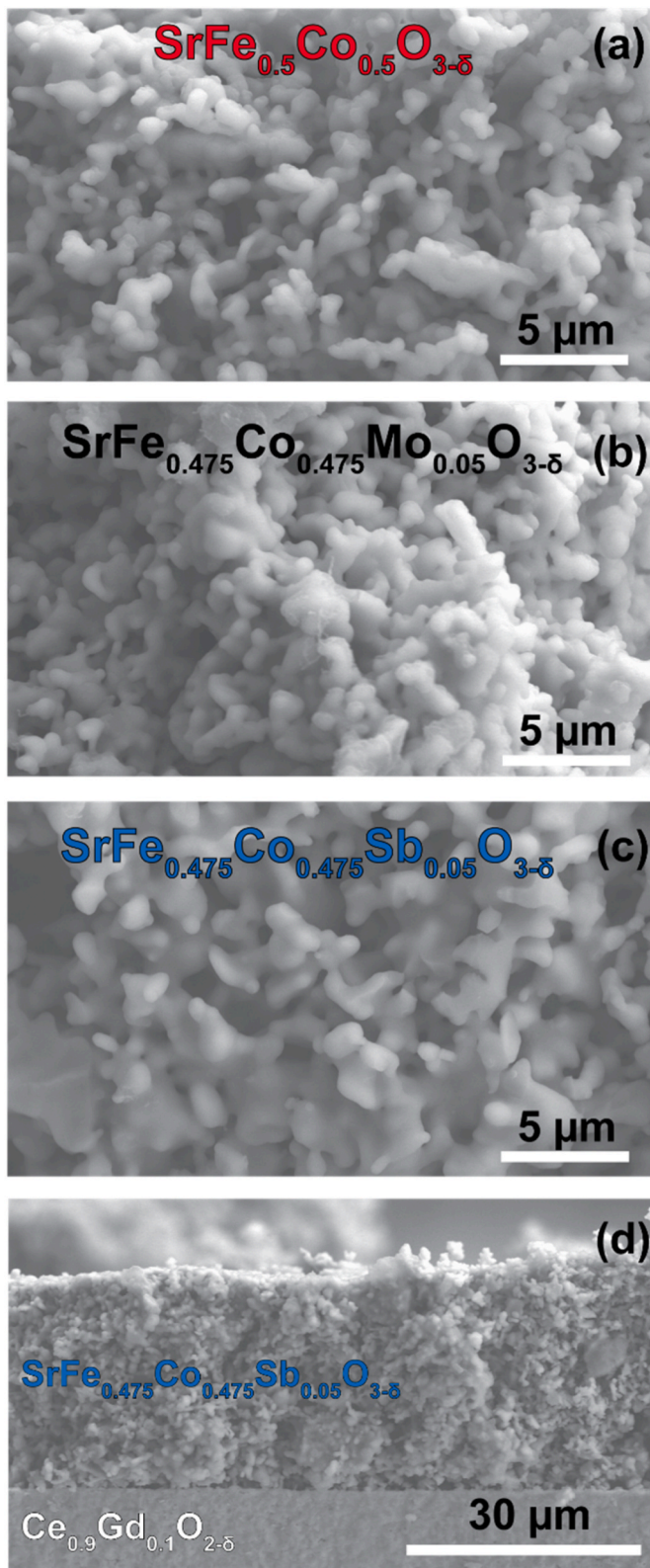
Fig. 2. SEM top-view images of (a) $SrFe_{0.5}Co_{0.5}O_{3-\delta}$, (b) $SrFe_{0.475}Co_{0.475}Mo_{0.05}O_{3-\delta}$ and (c) $SrFe_{0.475}Co_{0.475}Sb_{0.05}O_{3-\delta}$, and (d) cross-section view of $SrFe_{0.475}Co_{0.475}Sb_{0.05}O_{3-\delta}$ deposited over CGO electrolyte.

oxygen partial pressure [54]. Doping with both Mo and Sb increases the oxygen content, more significantly for Mo^{6+}. Moreover, the clear decrease of the content of larger trivalent cations $(Fe,Co)^{3+}$ on Mo doping is consistent with the slight contraction of the cell observed above. In contrast, Sb^{5+} species mainly replace the smaller $(Fe,Co)^{4+}$ cations; nevertheless, a similar trivalent cation content to the parent phase $SrFe_{0.5}Co_{0.5}O_{3-\delta}$ is retained. This is expected to produce cell expansion, as indicated by the higher lattice parameter of the Sb composition. Similar tendencies have been previously reported in the literature [50,55]. Compared to $SrFeO_{3-\delta}$, cobalt on the B-site increases the presence of the tetravalent state, associated with greater oxygen content and stabilisation of cubic symmetry at room temperature [44, 48]. The presence of 5 mol% Mo on the B site of the $SrFe_{0.5}Co_{0.5}O_{3-\delta}$ parent phase leads to a gain of oxygen content from 2.79 to 2.88, whereas our previous work showed that a higher Mo content of 10 mol% leads to a further increase of oxygen content to 2.94 [50]. In both cases Mo principally replaces Fe and Co in the trivalent state, increasing the average oxidation state of (Fe,Co).

The evolution of the oxygen content with temperature was obtained by thermogravimetry based on the RT data obtained from redox titration (Fig. 3). The behaviour of the three materials is similar, with no significant mass loss to ~300 °C, followed by a monotonous decrease due to thermal reduction of the B-site and the release of oxygen:

$$O_O^\times + 2B_B^\bullet \leftrightarrow \frac{1}{2}O_2 + v_0^{\bullet\bullet} + 2B_B^\times \qquad (1)$$

where O_O^X is an oxygen ion in its lattice site, $B_B^\bullet$ and $B_B^\times$ are B^{4+} and B^{3+} cations in the B position of the perovskite and $v_o^{\bullet\bullet}$ refers to the oxygen vacancy (Kröger-Vink notation). This response is typical of similar perovskite compositions [56–58]. The oxygen contents at 900 °C are 2.61, 2.71 and 2.59 for SFC, SFCM and SFCSb, respectively, indicating a more significant oxygen loss for SFCSb ($\Delta\delta = 0.23$ in the range RT-900 °C, compared to 0.18 and 0.17 for SFC and SFCM, respectively).

The thermal expansion curves of the materials studied in the range RT - 900 °C in air exhibit two regimes, with a lower slope in the lower temperature range followed by greater expansion rate in the higher temperature range (Fig. 4).

For SFCSb, the inflexion between the regimes is observed at ~385 °C, while for SFCM and SFC the change in regime occurs at ~550 and 650 °C, respectively. This leads to a higher value of thermal expansion coefficient (TEC) for the intermediate and high temperature range for the Sb-doped sample, as observed in Table 2. SFCM presents the most favourable thermal behaviour, maintaining a TEC of $14.9 \times 10^{-6}\,K^{-1}$ up to ~550 °C, which is compatible with common electrolytes such as CGO [59]. The three materials show comparable TEC values over the studied temperature range to those previously reported in the literature for parent compositions, as shown in Table 2. It is noteworthy that some dispersion of the TEC values is reported in the literature, probably because the lattice parameter and the thermal expansion may be affected by the oxygen stoichiometry and oxidation state of the cations, which are dependent on the processing route and thermal history.

The greater expansion of SFCSb is consistent with literature reports which show the impact of increasing the Sb content on the increase of TEC [24,62], whereas substitution with Mo leads to more moderate expansion [27,48,50]. The transition from the lower-slope to the higher-slope thermal regimes is also observed for parent compositions presented in Table 2 and is consistent with the mass loss observed in the TGA curves associated with the release of oxygen from the structure [58, 63,64], which increases both the degree of cation reduction and cell parameter as temperature rises. The greater oxygen release and corresponding TEC values may be more significant in Sb-doped compared to Mo-doped samples due to relatively weaker Sb-O bonds in comparison to Mo-O [65].

Table 1

Room-temperature average oxidation state (A.O.S) of (Fe,Co) cations determined by redox titration, and corresponding stoichiometric contents of $(Fe, Co)^{3+}$, $(Fe,Co)^{4+}$ and O^{2-} determined by electroneutrality (the oxidation state of molybdenum and antimony are assumed to be +6 and + 5, respectively).

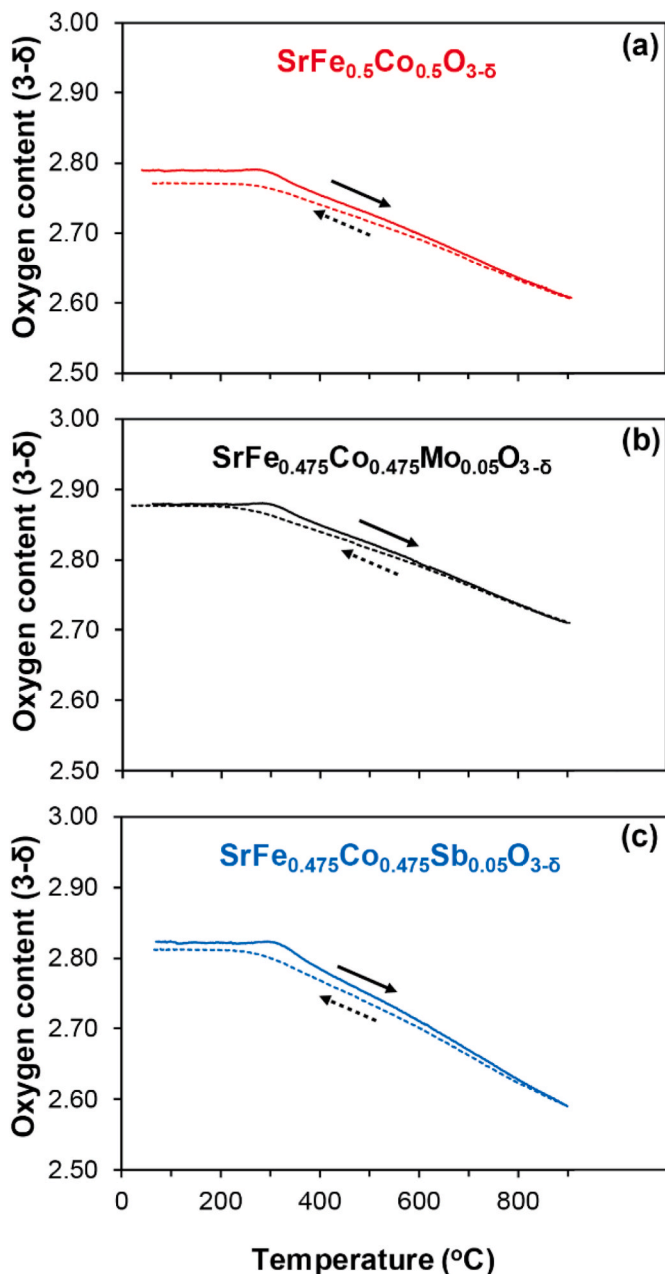| Material ($ABO_{3-\delta}$)	A. O. S	$[(Fe, Co)^{3+}]$	$[(Fe, Co)^{4+}]$	$[Mo^{6+}]$	$[Sb^{5+}]$	$[O^{2-}]$
$SrFe_{0.5}Co_{0.5}O_{3-\delta}$	3.57	0.43	0.57	-	-	2.79
$SrFe_{0.475}Co_{0.475}Mo_{0.05}O_{3-\delta}$	3.65	0.34	0.61	0.05	-	2.88
$SrFe_{0.475}Co_{0.475}Sb_{0.05}O_{3-\delta}$	3.56	0.42	0.53	-	0.05	2.82

Fig. 3. Oxygen content as a function of temperature (RT - 900 °C) obtained by redox titration and thermogravimetry in air for (a) $SrFe_{0.5}Co_{0.5}O_{3-\delta}$, (b) $SrFe_{0.475}Co_{0.475}Mo_{0.05}O_{3-\delta}$ and (c) $SrFe_{0.475}Co_{0.475}Sb_{0.05}O_{3-\delta}$.
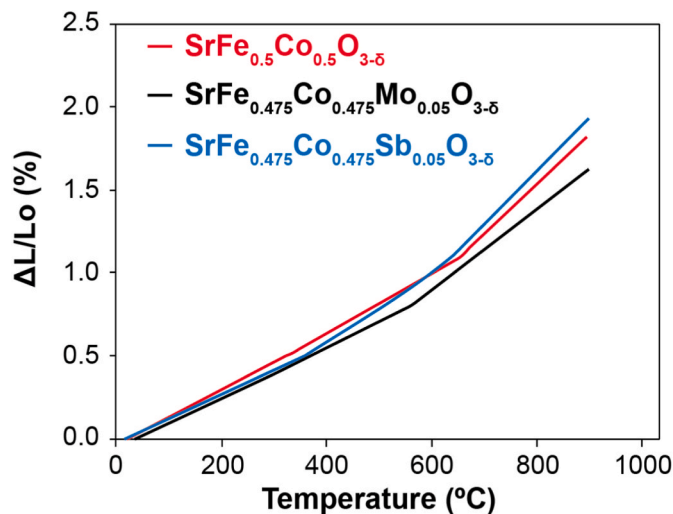

Fig. 4. Relative linear thermal expansion as a function of temperature of densified bars of $SrFe_{0.5}Co_{0.5}O_{3-\delta}$, $SrFe_{0.475}Co_{0.475}Mo_{0.05}O_{3-\delta}$ and $SrFe_{0.475}Co_{0.475}Sb_{0.05}O_{3-\delta}$.

3.3. Electrical conductivity

The electrical conductivity as a function of temperature is greater in oxygen than in air (Fig. 5) and a total conductivity maximum is observed in both atmospheres, characteristic of thermally activated electron-hole transport and variable carrier concentration. For temperatures lower than the maximum, conductivity increases as temperatures rises, due to a higher mobility of the electron-hole charge carriers, whereas, at higher temperature, oxygen is released (Fig. 3) [58,66], with loss of holes (Eq. (1)) and a corresponding decrease in conductivity.

The order of conductivity $\sigma_{SFCSb} < \sigma_{SFC} < \sigma_{SFCM}$ is mostly retained in the studied atmospheres and temperature range. The greater values of the Mo-containing sample are due to an increase in the proportion of electron holes residing as B^{4+} cations compared to the other compositions (Table 1), increasing the proportion of B^{3+} - O^{2-} - B^{4+} - O^{2-} - B^{3+} electronic conduction channels. The formation of such channels is less extensive in the case of Sb doping, with lower B^{4+} cation concentration and resultant lower conductivity, in agreement with literature reports [50,55]. In this regard, it has been reported that a low content of Sb doping (x = 0.05) is sufficient to stabilise the cubic perovskite phase in $SrCo_{1-x}Sb_xO_{3-\delta}$ [24], thus increasing the electrical conductivity; however, the increase of Sb content is detrimental to electrical transport. It is noteworthy that the total conductivity of SFCM presents maximum values of $\sigma_{MAX.}$~278 and 340 S cm^{-1} in air and oxygen, respectively, which are similar to those of similar compositions such as $SrFe_{0.4}Co_{0.6}O_{3-\delta}$ or $SrFe_{0.6}Co_{0.4}O_{3-\delta}$, which have peak conductivities of about 345 and 290 S cm^{-1} in air, respectively [46]. We note that the

Table 2

Thermal expansion coefficients (TEC) of the compositions studied in the current work (c.w.) compared to selected results of parent compounds reported in the literature.

Phase (ABO$_{3-\delta}$)	Atmosphere	TEC (x 10^{-6} K^{-1})	T range (ºC)	Reference
$SrFe_{0.5}Co_{0.5}O_{3-\delta}$	air	19.6	RT – 650	c.w.
		26.7	650 – 900	
$SrFe_{0.475}Co_{0.475}Mo_{0.05}O_{3-\delta}$	air	14.9	RT – 550	c.w.
		25.9	550 – 900	
$SrFe_{0.475}Co_{0.475}Sb_{0.05}O_{3-\delta}$	air	15.3	RT – 400	c.w.
		28.7	400 – 900	
$SrFe_{0.5}Co_{0.5}O_{3-\delta}$	argon	24.3	27 – 427	[60]
		53.0	427-627	
$SrFe_{0.1}Co_{0.9}O_{3-\delta}$	oxygen	28.4	50-850	[28]
$SrFe_{0.4}Co_{0.6}O_{3-\delta}$	air	23.8	RT-600	[49]
$SrFe_{0.45}Co_{0.45}Mo_{0.1}O_{3-\delta}$	air	14.8	RT – 400	[50]
		24.5	400 – 650	
$SrFe_{0.5}Co_{0.4}Nb_{0.1}O_{3-\delta}$	air	16.1	RT – 450	[61]
		24.4	450 – 900	
$SrCo_{0.95}Sb_{0.05}O_{3-\delta}$	air	15.2	200 – 400	[24]
		19.35	400 – 1000	
$SrCo_{0.95}Mo_{0.05}O_{3-\delta}$	air	17.2	RT – 450	[27]
		26.1	450 – 1000	
$SrFe_{0.8}Mo_{0.2}O_{3-\delta}$	air	25	800	[48]
$SrFe_{0.9}Mo_{0.1}O_{3-\delta}$	air	14.0	RT – 450	[44]
		29.3	500 – 900	
$SrFe_{0.95}Sb_{0.05}O_{3-\delta}$	air	10.6	27 – 582	[47]
		34.5	582 – 1000	
$SrFe_{0.8}Ta_{0.2}O_{3-\delta}$	air	14.5	RT – 400	[36]
		21.6	400 – 1000	

Fig. 5. Electrical conductivity as a function of temperature for $SrFe_{0.5}Co_{0.5}O_{3-\delta}$ (circles), $SrFe_{0.475}Co_{0.475}Mo_{0.05}O_{3-\delta}$ (triangles) and $SrFe_{0.475}Co_{0.475}Sb_{0.05}O_{3-\delta}$ (squares) under (a) air and (b) oxygen.

current results are also comparable or even higher than those previously reported for perovskites with significantly higher Co contents, such as ~300 S cm^{-1} for $SrCo_{0.9}Sb_{0.1}O_{3-\delta}$ [24] or ~ 286 and ~170 S cm^{-1} for $SrCo_{0.95}Mo_{0.05}O_{3-\delta}$ and $SrCo_{0.9}Mo_{0.1}O_{3-\delta}$, respectively [67].

3.4. Electrochemical analysis

Fig. 6(a) presents a comparison of typical impedance spectra in air of the three electrodes over CGO electrolyte in half-cell configuration at 700 °C. The electrode area-specific resistance (ASR) for SFC, SFCM and SFCSb are 0.38, 0.28 and 0.10 Ω cm^2 at 700 °C, respectively. These results confirm that the presence of cobalt in $SrFeO_{3-\delta}$–based systems improves the electrochemical performance in comparison to the Co-free composition, prepared in a similar way [50], with a value of ASR ~ 0.55 Ω cm^2 at 700 °C. Fig. 6(b) shows the corresponding Arrhenius plots in the range 600-900 °C, where Mo- and Sb-doping improves the electrochemical reaction in the order ASR$_{SFC}$ > ASR$_{SFCM}$ > ASR$_{SFCSb}$. The Sb-doped electrode response is particularly promising, with comparable ASR values to perovskite materials with significantly more cobalt content on the B site, such as $SrCo_{0.95}Sb_{0.05}O_{3-\delta}$ with an ASR ~0.06 Ω cm^2 [24], $SrCo_{0.9}Mo_{0.1}O_{3-\delta}$ with ASR ~ 0.16 Ω cm^2 [27], $SrCo_{0.95}Ti_{0.05}O_{3-\delta}$ with ASR ~ 0.18 Ω cm^2 [64], and $SrCo_{0.9}Nb_{0.1}O_{3-\delta}$ with ASR ~ 0.083 Ω cm^2 [68], at 700 °C, or with the presence of a rare-earth cation on the A site, such as $Sr_{0.7}Y_{0.3}CoO_{3-\delta}$, $La_{0.6}Sr_{0.4}Co_{0.2}Fe_{0.8}O_{3-\delta}$ or $Nd_{0.75}Sr_{0.25}Co_{0.8}Fe_{0.2}O_{3-\delta}$, with respective ASR values of ~1, 0.3 and 0.2 Ω cm^2 at 700 °C [69–71]. It should be mentioned that the literature data report a wide range of dispersion among similar families of compounds and comparisons should be made with care, given that the
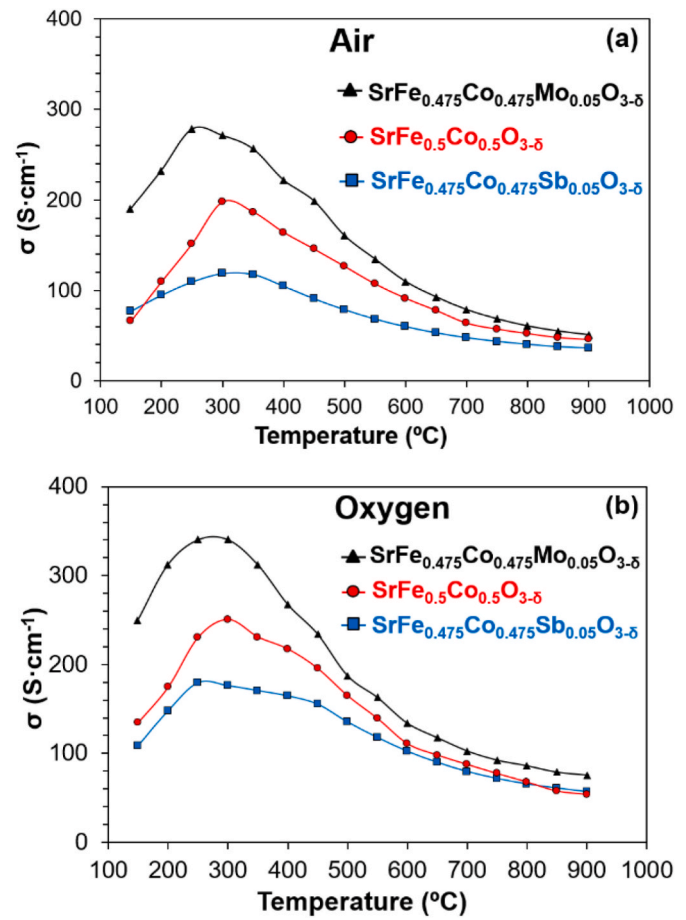
air-electrode electrochemical performance is highly dependent on the processing route and thermal history, which not only affects the oxidation states of the cations but also the microstructure and stability of the air electrodes.

Impedance spectra were fitted to equivalent circuits composed of several series components, typically L-R$_s$-(RQ)$_{HF}$-(RQ)$_{LF}$, where L is introduced to account for the autoinductive process of the experimental setup, R$_s$ accounts for the ohmic contribution, and each (RQ)$_i$ term corresponds to a resistance and a pseudocapacitance connected in parallel, introduced to fit the high-frequency ((RQ)$_{HF}$) and low-frequency ((RQ)$_{LF}$) electrochemical processes. Fig. 7 shows the results obtained at 800 °C for the compositions studied in the current work. Although the fitting of the spectra according to the equivalent circuits is mathematically accurate, the analysis should be performed with care, given that the oxygen electrochemical processes overlap considerably. The results indicate that the high-frequency process, which is associated to diffusion of oxide ions in the bulk phase [72], is characterised by capacitances of the order of 10^{-3}-10^{-2} F, whereas the low-frequency processes, associated to the oxygen surface interchange, exhibit capacitances of 10^{-1}-10^0 F. In mixed-conducting cathodes, the electrochemical reaction is dominated by the bulk pathway [73], and a high performance requires fast oxygen exchange reactions and fast bulk chemical diffusion [74–76]. Oxygen vacancies often play the dominant role in the surface exchange process; however, they also play a key role in the oxygen bulk diffusion, because high ionic (and electronic) conductivity is required for efficient oxygen transport. Fig. 7(d) shows that although Mo doping has a minor influence on the electrode performance, Sb doping reduces considerably the area-specific resistance corresponding to both the high-frequency
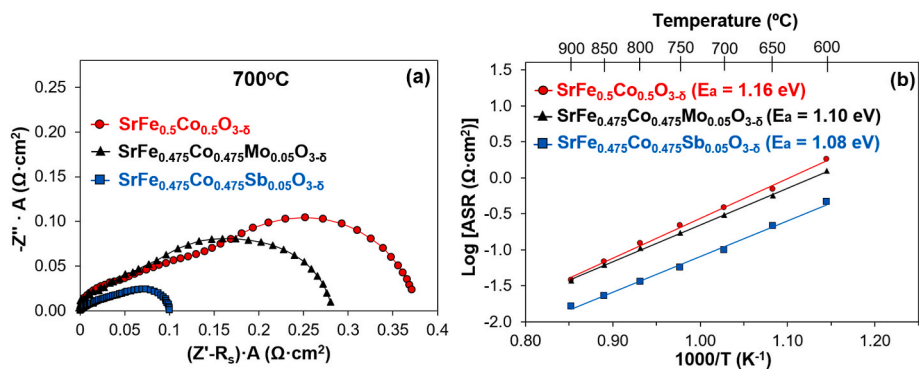
Fig. 6. (a) Impedance spectra obtained without dc polarisation at 700 °C and (b) Arrhenius representation of area-specific resistance of the oxygen electrochemical process in air for $SrFe_{0.5}Co_{0.5}O_{3-\delta}$ (circles), $SrFe_{0.475}Co_{0.475}Mo_{0.05}O_{3-\delta}$ (triangles) and $SrFe_{0.475}Co_{0.475}Sb_{0.05}O_{3-\delta}$ (squares) in a half-cell based on CGO electrolyte. Note that the spectra represented in (a) are displaced to the origin of the real axis for a clearer comparison of the electrode-electrolyte electrochemical process.
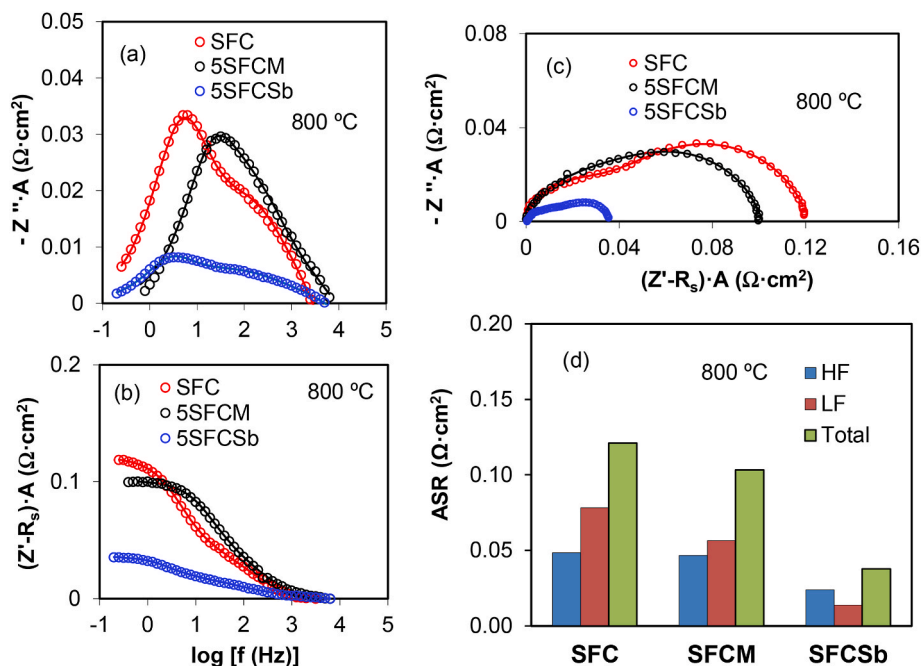

Fig. 7. (a), (b) and (c) Representation of experimental impedance spectra (open circles) and corresponding fittings (continuous lines), according to the equivalent circuits, at 800 °C; (d) results of area-specific resistances at 800 °C associated to the high-frequency (HF), low-frequency (LF) and overall oxygen electrochemical processes.

and the low-frequency electrochemical processes. It is likely that a greater oxygen-vacancy content with temperature for the Sb-doped sample in comparison to the Mo-doped electrode is beneficial for the oxygen exchange reaction and oxygen-ion diffusion, although other factors such as hole and oxide-ion mobility, hole content and cation segregation at the surface may come into play in the observed order.

The effect of dc bias on the normalised electrode polarisation resistance is shown in Fig. 8. The results show analogous behaviour to that previously reported for similar compositions [25,44,50]. As a general trend, the electrode polarisation resistance is not substantially affected by the magnitude of the direct current at high temperature, but decreases considerably as the direct current increases at lower temperature. The oxygen reduction/oxidation reactions in mixed conducting air electrodes are affected by oxygen surface exchange and oxide-ion bulk diffusion [74,75]. The oxygen bulk diffusion and oxygen surface exchange in cathodic polarisation are dominated by oxygen vacancies [75], whereas oxygen surface exchange in anodic polarisation should be dominated by concentration of oxide ions at surface reaction sites, which are required to evolve oxygen. In the high temperature range,

both the oxygen surface exchange and the oxygen bulk diffusion are faster, and only minor further modification of oxygen vacancies and oxide ions at reaction sites occur as the direct current is increased. However, for lower temperatures, the oxygen surface exchange and the oxygen bulk diffusion decrease considerably such that the oxygen-vacancy content and oxide ions at reaction sites are affected more considerably for high cathodic and anodic currents, respectively, decreasing the electrode polarisation resistance. The three materials generally show a better response under anodic polarisation, as observed previously for similar systems [25,50,77], most likely because oxygen exchange limitation is expected to have a greater effect on the electrochemical performance for oxygen adsorption under cathodic polarisation, in comparison to oxygen evolution under anodic polarisation [50,78,79].

Fig. 9 shows that the cathodic and anodic overpotentials are lower for the Sb-doped sample in comparison to the Mo-doped and undoped compositions, in good agreement with the lower electrode polarisation resistance of the former (Fig. 6). On the other hand, differences are lower in the high current range, due to the marked improvement of the
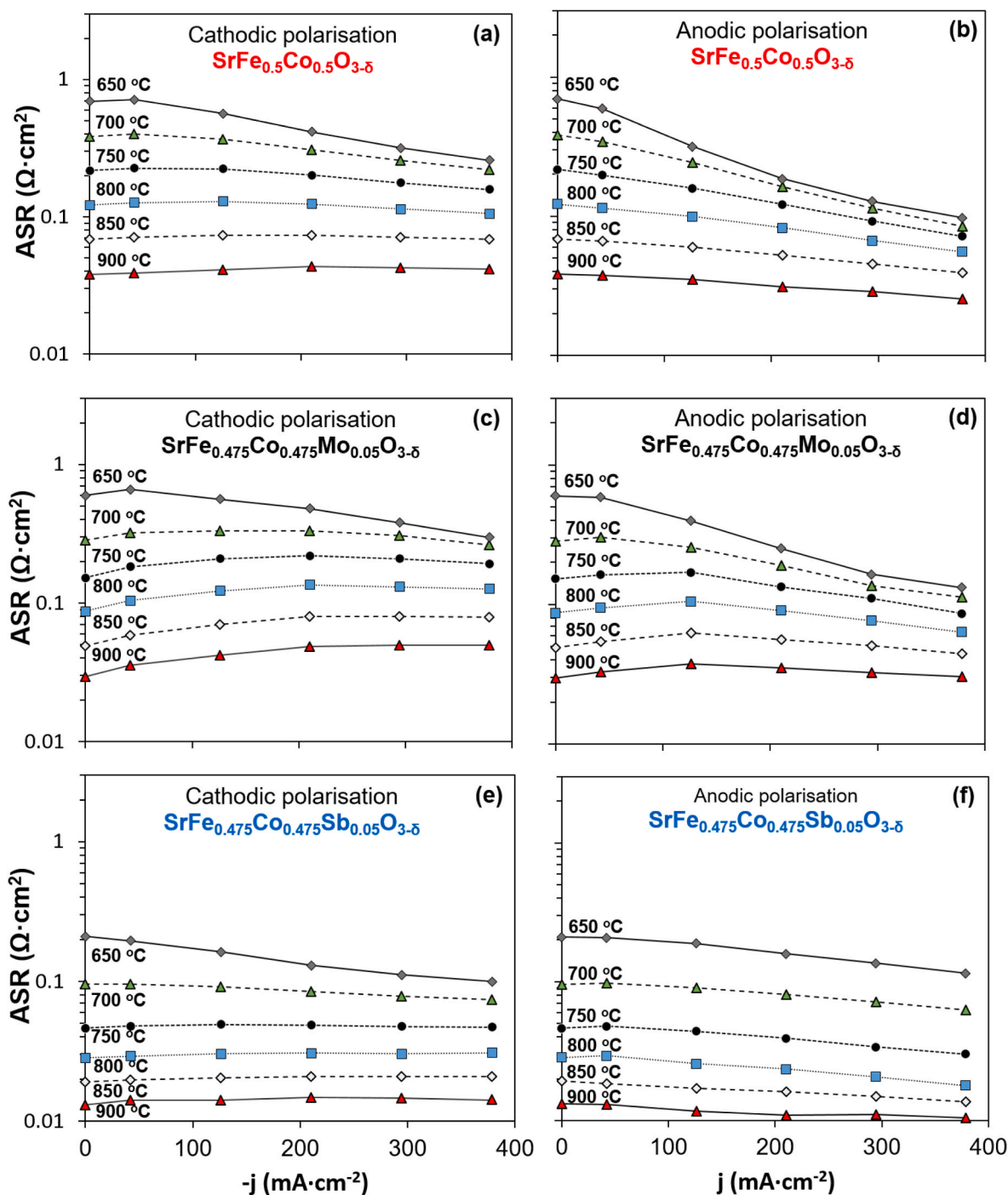
Fig. 8. Modification of ASR by direct current in cathodic polarisation (a, c, e) and anodic polarisation (b, d, f) for $SrFe_{0.5}Co_{0.5}O_{3-\delta}$ (a, b), $SrFe_{0.475}Co_{0.475}Mo_{0.05}O_{3-\delta}$ (c, d) and $SrFe_{0.475}Co_{0.475}Sb_{0.05}O_{3-\delta}$ (e, f).

electrochemical performance for SFC and SFCM.

3.5. Stability

The electrochemical stability of the electrode-electrolyte half-cell assemblies was evaluated o thermal cycling (Fig. 10), showing good stability of the ASR for Sb- and Mo-doped samples but a greater increase for the undoped SFC composition. The more pronounced deterioration of the electrochemical response of the SFC sample on cycling with temperature may be attributable to a greater thermal expansion at intermediate temperature (Table 2) and degradation at the electrode-electrolyte interface [80].

However, in terms of relative degradation after 10 thermal cycles, the SFCSb electrode presents the highest relative increase of electrode polarisation resistance (~36%) in comparison to the SFC (~29%) and SFCM (~14%) electrodes. Further optimisation of these promising electrodes is warranted to improve component compatibility and limit degradation associated with expansion. Attention may be paid to microstructural modification with alternative synthesis routes such as spray pyrolysis, allowing a lower synthesis temperature and smaller grain size [44], and the deposition of intermediate layers between the electrode and electrolyte [81,82].
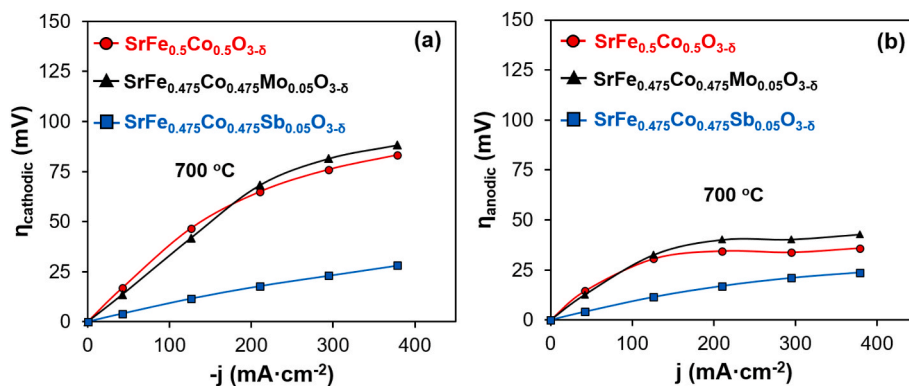
Fig. 9. Effect of cathodic (a) and anodic (b) direct current density on the overpotential at the working electrode for SFC, SFCM and SFCSb over CGO electrolyte.
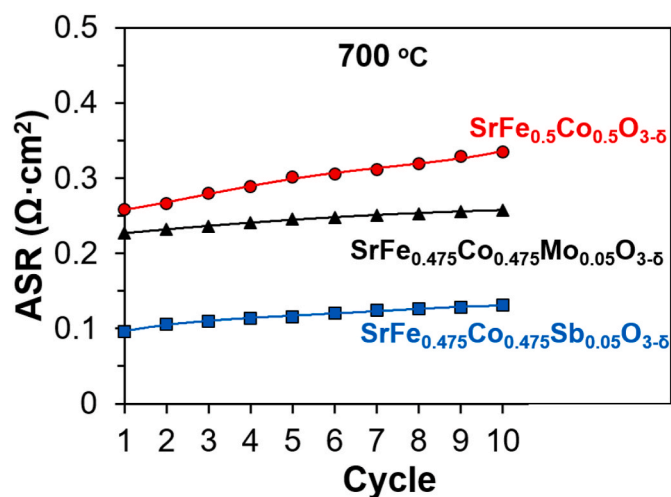

Fig. 10. Area-specific resistance at 700 °C as a function of the number of heating/cooling cycles.

4. Conclusions

Substitution on the perovskite B site of the intermediate-temperature solid oxide cell air electrode material $SrFe_{0.5}Co_{0.5}O_{3-\delta}$ with minor amounts (5 mol%) of either Mo or Sb has significant and differing influences on oxygen content, thermal behaviour and electrochemical properties.

The introduction of molybdenum with a final firing temperature of 1000 °C increases both stoichiometric oxygen and the concentration of electron holes localised as B^{4+} cations, resulting in higher conductivity (340 S cm^{-1} at 300 °C in O_2). In addition, the stability of the electrochemical response of half cells of the Mo-doped electrodes and CGO electrolyte on thermal cycling improves in comparison to half cells with the $SrFe_{0.5}Co_{0.5}O_{3-\delta}$ parent phase, most probably related to a more moderate TEC value at intermediate temperature, with better compatibility with the CGO electrolyte.

Doping with 5 mol % Sb requires a synthesis temperature of 1100 °C to achieve phase-pure perovskite. The Sb-containing phase exhibits a greater oxygen-vacancy content than the Mo-doped phase at room temperature, and also greater oxygen loss with increasing temperature. The more significant oxygen-vacancy content is associated with a lower electron-hole charge-carrier concentration, leading to a lower conductivity than the other studied compositions. However, the high oxygen-vacancy content significantly improves the electrochemical performance, and ASR values comparable with perovskites of much higher cobalt content are achieved. All three studied materials are competitive as air electrodes for intermediate temperature solid oxide cells,

warranting further study targeted on improving microstructure and component compatibility.

References

[1] EG&G Technical Services, Inc, "Fuel Cell Handbook" U.S. Department of Energy, seventh ed., 2004.

[2] M. Singh, D. Zappa, E. Comini, Solid oxide fuel cell: decade of progress, future perspectives and challenges, Int. J. Hydrogen Energy 46 (2021) 27643–27674, https://doi.org/10.1016/J.IJHYDENE.2021.06.020.

[3] M. Burer, K. Tanaka, D. Favrat, K. Yamada, Multi-criteria optimization of a district cogeneration plant integrating a solid oxide fuel cell–gas turbine combined cycle, heat pumps and chillers, Energy 28 (2003) 497–518, https://doi.org/10.1016/S0360-5442(02)00161-5.

[4] F. Ramadhani, M.A. Hussain, H. Mokhlis, S. Hajimolana, Optimization strategies for solid oxide fuel cell (SOFC) application: a literature survey, Renew. Sustain. Energy Rev. 76 (2017) 460–484, https://doi.org/10.1016/j.rser.2017.03.052.

[5] A. Kasaeian, M. Javidmehr, M.R. Mirzaie, L. Fereidooni, Integration of solid oxide fuel cells with solar energy systems: a review, Appl. Therm. Eng. 224 (2023), 120117, https://doi.org/10.1016/J.APPLTHERMALENG.2023.120117.

[6] M.A. Laguna-Bercero, Recent advances in high temperature electrolysis using solid oxide fuel cells: a review, J. Power Sources 203 (2012) 4–16, https://doi.org/10.1016/j.jpowsour.2011.12.019.

[7] A. Nechache, M. Cassir, A. Ringuedé, Solid oxide electrolysis cell analysis by means of electrochemical impedance spectroscopy: a review, J. Power Sources 258 (2014) 164–181, https://doi.org/10.1016/j.jpowsour.2014.01.110.

[8] A. Hauch, R. Küngas, P. Blennow, A.B. Hansen, J.B. Hansen, B.V. Mathiesen, M. B. Mogensen, Recent advances in solid oxide cell technology for electrolysis, Science 370 (2020), eaba6118, https://doi.org/10.1126/SCIENCE.ABA6118.

[9] W. Zhang, M. Liu, X. Gu, Y. Shi, Z. Deng, N. Cai, Water electrolysis toward elevated temperature: advances, challenges and frontiers, Chem. Rev. 123 (2023) 7119–7192, https://doi.org/10.1021/ACS.CHEMREV.2C00573.

[10] Y. Zheng, Z. Chen, J. Zhang, Solid oxide electrolysis of H_2O and CO_2 to produce hydrogen and low-carbon fuels, Electrochem. Energy Rev. 4 (2021) 508–517, https://doi.org/10.1007/s41918-021-00097-4.

[11] D.J.L. Brett, A. Atkinson, N.P. Brandon, S.J. Skinner, Intermediate temperature solid oxide fuel cells, Chem. Soc. Rev. 37 (2008) 1568–1579, https://doi.org/10.1039/B612060C.

[12] M.B. Mogensen, Materials for reversible solid oxide cells, Curr. Opin. Electrochem. 21 (2020) 265–273, https://doi.org/10.1016/j.coelec.2020.03.014.

[13] C. Duan, R. Kee, H. Zhu, N. Sullivan, L. Zhu, L. Bian, D. Jennings, R. O'Hayre, Highly efficient reversible protonic ceramic electrochemical cells for power generation and fuel production, Nat. Energy 4 (2019) 230–240, https://doi.org/10.1038/s41560-019-0333-2.

[14] S.B. Adler, Factors governing oxygen reduction in solid oxide fuel cell cathodes, Chem. Soc. Rev. 104 (2004) 4791–4844, https://doi.org/10.1021/cr020724o.

[15] A. Ndubuisi, S. Abouali, K. Singh, V. Thangadurai, Recent advances, practical challenges, and perspectives of intermediate temperature solid oxide fuel cell cathodes, J. Mater. Chem. A 10 (2022) 2196–2227, https://doi.org/10.1039/d1ta08475e.

[16] A.P. Tarutin, E.A. Filonova, S. Ricote, D.A. Medvedev, Z. Shao, Chemical design of oxygen electrodes for solid oxide electrochemical cells: a guide, Sustain. Energy Technol. Assessments 57 (2023), 103185, https://doi.org/10.1016/J.SETA.2023.103185.

[17] C. Chun, J.A. Alonso, J. Bian, Recent advances in perovskite-type oxides for energy conversion and storage applications, Adv. Energy Mater. 11 (2021), 2000459, https://doi.org/10.1002/aenm.202000459.

[18] S.P. Jiang, Development of lanthanum strontium manganite perovskite cathode materials of solid oxide fuel cells: a review, J. Mater. Sci. 43 (2008) 6799–6833, https://doi.org/10.1007/s10853-008-2966-6.

[19] S.P. Jiang, Development of lanthanum strontium cobalt ferrite perovskite electrodes of solid oxide fuel cells – a review, Int. J. Hydrogen Energy 44 (2019) 7448–7493, https://doi.org/10.1016/j.ijhydene.2019.01.212.

[20] L. Baldi, M. Peri, D. Vandone, Clean energy industries and rare earth materials: economic and financial issues, Energy Pol. 66 (2014) 53–61, https://doi.org/10.1016/j.enpol.2013.10.067.

[21] J.H. Fan, A. Omura, E. Roca, Geopolitics and rare earth metals, Eur. J. Polit. Econ. 78 (2023), 102356, https://doi.org/10.1016/j.ejpoleco.2022.102356.

[22] Z.-Z. Li, Q. Meng, L. Zhang, O.-R. Lobont, Y. Shen, How do rare earth prices respond to economic and geopolitical factors? Resour. Pol. 85 (2023) 103853 https://doi.org/10.1016/j.resourpol.2023.103853.

[23] V. Cascos, R. Martínez-Coronado, J.A. Alonso, New Nb-doped SrCo$_{1-x}$Nb$_x$O$_{3-\delta}$ perovskites performing as cathodes in solid-oxide fuel cells, Int. J. Hydrogen Energy 39 (2014) 14349–14354, https://doi.org/10.1016/j.ijhydene.2014.03.100.

[24] A. Aguadero, D. Pérez-Coll, C. de la Calle, J.A. Alonso, M.J. Escudero, L. Daza, SrCo$_{1-x}$Sb$_x$O$_{3-\delta}$ perovskite oxides as cathode materials in solid oxide fuel cells, J. Power Sources 192 (2009) 132–137, https://doi.org/10.1016/j.jpowsour.2008.12.138.

[25] J. Wang, T. Yang, L. Lei, K. Huang, Ta-doped SrCoO$_{3-\delta}$ as a promising bifunctional oxygen electrode for reversible solid oxide fuel cells: a focused study on stability, J. Mater. Chem. A 5 (2017) 8989–9002, https://doi.org/10.1039/C7TA02003A.

[26] P.Y. Zeng, R. Ran, Z.H. Chen, W. Zhou, H.X. Gu, Z.P. Shao, S.M. Liu, Efficient stabilization of cubic perovskite SrCoO$_{3-\delta}$ by B-site low concentration scandium doping combined with sol–gel synthesis, J. Alloys Compd. 455 (2008) 465–470, https://doi.org/10.1016/j.jallcom.2007.01.144.

[27] A. Aguadero, D. Pérez-Coll, J.A. Alonso, S.J. Skinner, J. Kilner, A new family of Mo-doped SrCoO$_{3-\delta}$ perovskites for application in reversible solid state electrochemical cells, Chem. Mater. 24 (2012) 2655–2663, https://doi.org/10.1021/cm300255r.

[28] T. Nagai, W. Ito, T. Sakon, Relationship between cation substitution and stability of perovskite structure in SrCoO$_{3-\delta}$-based mixed conductors, Solid State Ionics 177 (2007) 3433–3444, https://doi.org/10.1016/j.ssi.2006.10.022.

[29] M. Li, M. Zhao, F. Li, W. Zhou, V.K. Peterson, X. Xu, Z. Shao, I. Gentle, Z. Zhu, A niobium and tantalum co-doped perovskite cathode for solid oxide fuel cells operating below 500 °C, Nat. Commun. 8 (2017), 13990, https://doi.org/10.1038/ncomms13990.

[30] S.W.D. Gourley, T. Or, Z. Chen, Breaking free from cobalt reliance in lithium-ion batteries, iScience 23 (2020), 101505, https://doi.org/10.1016/j.isci.

[31] M. Grohol, C. Veeh, DG Grow, European Commission, Study on the Critical Raw Materials for the EU 2023: Final Report, https://doi.org/10.2873/725585.

[32] S. McIntosh, J.F. Vente, W.G. Haije, D.H.A. Blank, H.J.M. Bouwmeester, Phase stability and oxygen non-stoichiometry of SrCo$_{0.8}$Fe$_{0.2}$O$_{3-\delta}$ measured by in situ neutron diffraction, Solid State Ionics 177 (2006) 833–842, https://doi.org/10.1016/j.ssi.2006.02.017.

[33] I.V. Belenkaya, A.A. Matvienko, A.P. Nemudry, Phase transitions and microstructure of ferroelastic MIEC oxide SrCo$_{0.8}$Fe$_{0.2}$O$_{2.5}$ doped with highly charged Nb/Ta(V) cations, J. Mater. Chem. A 3 (2015) 23240–23251, https://doi.org/10.1039/C5TA06581J.

[34] S. Kumar, A. Das, S. Omar, Electrochemical performance of SrFeO$_{3-\delta}$ for application as a symmetric electrode in solid oxide fuel cells, ACS Appl. Energy Mater. 6 (2023) 2049–2062, https://doi.org/10.1021/ACSAEM.2C04034.

[35] L. Dos Santos-Gómez, J.M. Porras-Vázquez, E.R. Losilla, D. Marrero-López, Ti-doped SrFeO$_3$ nanostructured electrodes for symmetric solid oxide fuel cells, RSC Adv. 5 (2015) 107889–107895, https://doi.org/10.1039/c5ra23771h.

[36] C. Yao, H. Zhang, Y. Dong, R. Zhang, J. Meng, F. Meng, Characterization of Ta/W co-doped SrFeO$_{3-\delta}$ perovskite as cathode for solid oxide fuel cells, J. Alloys Compd. 797 (2019) 205–212, https://doi.org/10.1016/j.jallcom.2019.05.096.

[37] M.P. Pechini, Method of Preparing Lead and Alkaline Earth Titanates and Niobates and Coating Method Using the Same to Form a Capacitor, US Pat, 1967 (n.d.).

[38] J. Rodríguez-Carvajal, Recent advances in magnetic structure determination by neutron powder diffraction, Phys. B Condens. Matter 192 (1993) 55–69, https://doi.org/10.1016/0921-4526(93)90108-I.

[39] M. Yuste, J.C. Pérez-Flores, J.R. de Paz, M.T. Azcondo, F. García-Alvarado, U. Amador, New perovskite materials of the La$_{2-x}$Sr$_x$CoTiO$_6$ series, Dalton Trans. 40 (2011) 7908, https://doi.org/10.1039/c1dt10196j.

[40] M.S. Alam, I. Kagomiya, K. Kakimoto, Tailoring the oxygen permeability of BaCo$_{0.4}$Fe$_{0.4}$Y$_{0.2-x}$A$_x$O$_{3-\delta}$ (x= 0, 0.1; A: Zr, Mg, Zn) cubic perovskite, Ceram. Int. 49 (2023) 11368–11377, https://doi.org/10.1016/j.ceramint.2022.11.336.

[41] P. Ciambelli, S. Cimino, L. Lisi, M. Faticanti, G. Minelli, I. Pettiti, P. Porta, La, Ca and Fe oxide perovskites: preparation, characterization and catalytic properties for methane combustion, Appl. Catal., B 33 (2001) 193–203, https://doi.org/10.1016/S0926-3373(01)00163-1.

[42] D. Pérez-Coll, A. Aguadero, M.J. Escudero, P. Núñez, L. Daza, Optimization of the interface polarization of the La$_2$NiO$_4$-based cathode working on the Ce$_{1-x}$Sm$_x$O$_{2-\delta}$ electrolyte system, J. Power Sources 178 (2008) 151–162, https://doi.org/10.1016/j.jpowsour.2007.12.030.

[43] D. Pérez-Coll, A. Aguadero, M.J. Escudero, L. Daza, Effect of DC current polarization on the electrochemical behaviour of La$_2$NiO$_{4+\delta}$ and La$_3$Ni$_2$O$_{7+\delta}$-based systems, J. Power Sources 192 (2009) 2–13, https://doi.org/10.1016/j.jpowsour.2008.10.073.

[44] V. Zapata-Ramírez, P. Rosendo-Santos, U. Amador, C. Ritter, G.C. Mather, D. Pérez-Coll, Optimisation of high-performance, cobalt-free SrFe$_{1-x}$Mo$_x$O$_{3-\delta}$ cathodes for solid oxide fuel cells prepared by spray pyrolysis, Renew. Energy 185 (2022) 1167–1176, https://doi.org/10.1016/j.renene.2021.12.121.

[45] T.V. Aksenova, L.Ya Gavrilova, V.A. Cherepanov, Phase equilibria and crystal structure of the complex oxides in the Sr–Fe–Co–O system, J. Solid State Chem. 181 (2008) 1480–1484, https://doi.org/10.1016/j.jssc.2008.03.010.

[46] Z. Wang, Z. Zhao, N. Xy, Y. Shen, W. Ding, X. Lu, F. Li, Electrical conductivity and structural stability of SrCo$_{1-x}$Fe$_x$O$_{3-\delta}$, J. Phys. Chem. Solid. 72 (2011) 50–55, https://doi.org/10.1016/j.jpcs.2010.09.084.

[47] Y. Meng, L. Sun, J. Gao, W. Tan, C. Chen, J. Yi, H.J.M. Bouwmeester, Z. Sun, K. S. Brinkman, Insights into the CO$_2$ stability-performance trade-off of antimony-doped SrFeO$_{3-\delta}$ perovskite cathode for solid oxide fuel cells, ACS Appl. Mater. Interfaces 11 (2019) 11498–11506, https://doi.org/10.1021/ACSAMI.9B00876.

[48] G. Xiao, Q. Liu, S. Wang, V.G. Komvokis, M.D. Amiridis, A. Heyden, S. Ma, F. Chen, Synthesis and characterization of Mo-doped SrFeO$_{3-\delta}$ as cathode materials for solid oxide fuel cells, J. Power Sources 202 (2012) 63–69, https://doi.org/10.1016/j.jpowsour.2011.11.021.

[49] Y. Chen, B. Qian, Z. Shao, Tin and iron co-doping strategy for developing active and stable oxygen reduction catalysts from SrCoO$_{3-\delta}$ for operating below 800 °C, J. Power Sources 294 (2015) 339–346, https://doi.org/10.1016/j.jpowsour.2015.06.095.

[50] V. Zapata-Ramírez, G.C. Mather, M.T. Azcondo, U. Amador, D. Pérez-Coll, Electrical and electrochemical properties of the Sr(Fe,Co,Mo)O$_{3-\delta}$ system as air electrode for reversible solid oxide cells, J. Power Sources 437 (2019), 226895, https://doi.org/10.1016/j.jpowsour.2019.226895.

[51] N. Mushtaq, C. Xia, W. Dong, G. Abbas, R. Raza, A. Ali, S. Rauf, B. Wang, J.-S. Kim, B. Zhu, Perovskite SrFe$_{1-x}$Ti$_x$O$_{3-\delta}$ (x < = 0.1) cathode for low temperature solid oxide fuel cell, Ceram. Int. 44 (2018) 10266–10272, https://doi.org/10.1016/j.ceramint.2018.03.033.

[52] A. Demont, R. Sayers, M.A. Tsiamtsouri, S. Romani, P.A. Chater, H. Niu, C. Martí-Gastaldo, Z. Xu, Z. Deng, Y. Bréard, M.F. Thomas, J.B. Claridge, M.J. Rosseinsky, Single sublattice endotaxial phase separation driven by charge frustration in a complex oxide, J. Am. Chem. Soc. 135 (2013) 10114–10123, https://doi.org/10.1021/ja403611s.

[53] G.V. Bazuev, A.P. Tyutyunnik, A.V. Korolev, E. Suard, C.W. Tai, N.V. Tarakina, The effect of manganese oxidation state on antiferromagnetic order in SrMn$_{1-x}$Sb$_x$O$_3$ (0 < x < 0.5) perovskite solid solutions, J. Mater. Chem. C 7 (2019) 2085–2095, https://doi.org/10.1039/C8TC05717F.

[54] J. Rager, M. Zipperle, A. Sharma, J.L. MacManus-Driscoll, Oxygen stoichiometry in Sr$_2$FeMoO$_6$, the determination of Fe and Mo valence states, and the chemical phase diagram of SrO-Fe$_3$O$_4$-MoO$_3$, J. Am. Ceram. Soc. 87 (2004) 1330–1335, https://doi.org/10.1111/J.1151-2916.2004.TB07730.X.

[55] X. Xie, Y. Xie, Y. Wan, Y. Yang, X. Wu, C. Xia, Antimony-doped strontium cobalt oxide as promising cathode for low-temperature solid oxide fuel cell with excellent carbon dioxide tolerance, Appl. Catal., B: Environmental, Appl. Catal. B 286 (2021), 119901, https://doi.org/10.1016/j.apcatb.2021.119901.

[56] Y. Gou, G. Li, R. Ren, C. Xy, J. Qiao, W. Sun, K. Sun, Z. Wang, Pr-Doping motivating the phase transformation of the BaFeO$_{3-\delta}$ perovskite as a high-performance solid oxide fuel cell cathode, ACS Appl. Mater. Interfaces 13 (2021) 20174–20184, https://doi.org/10.1021/acsami.1c03514.

[57] D. Muñoz-Gil, M.T. Azcondo, C. Ritter, O. Fabelo, D. Pérez-Coll, G.C. Mather, U. Amador, K. Boulahya, The Effects of Sr Content on the Performance of Nd$_{1-x}$Sr$_x$CoO$_{3-\delta}$ air electrode materials for intermediate temperature solid oxide fuel cells under operational conditions, Inorg. Chem. 59 (2020) 12111–12121, https://doi.org/10.1021/acs.inorgchem.0c01049.

[58] L. dos Santos-Gómez, J.M. Campana, S. Bruque, E.R. Losilla, D. Marrero-López, Symmetric electrodes for solid oxide fuel cells based on Zr-doped SrFeO$_{3-\delta}$, J. Power Sources 279 (2015) 419–427, https://doi.org/10.1016/j.jpowsour.2015.01.043.

[59] S. Omar, J.C. Nino, Consistency in the chemical expansion of fluorites: a thermal revision of the doped ceria, Acta Mater. 61 (2013) 5406–5413, https://doi.org/10.1016/j.actamat.2013.05.029.

[60] M.J. Shin, J.H. Yu, Oxygen transport of A-site deficient Sr$_{1-x}$Fe$_{0.5}$Co$_{0.5}$O$_{3-\delta}$ (x = 0–0.3) membranes, J. Membr. Sci. 401–402 (2012) 40–47, https://doi.org/10.1016/j.memsci.2012.01.023.

[61] Y. Zhu, J. Sunarso, W. Zhou, S. Jiang, Z. Shao, High-performance SrNb$_{0.1}$Co$_{0.9-x}$Fe$_x$O$_{3-\delta}$ perovskite cathodes for low-temperature solid oxide fuel cells, J. Mater. Chem. A 2 (2014) 15454–15462, https://doi.org/10.1039/C4TA03208J.

[62] N. Mushtaq, Y. Lu, C. Xia, W. Dong, B. Wang, X. Wang, M.A.K. Yousaf Shah, S. Rauf, N. Jingjing, E. Hu, H. Xiao, R. Raza, J.-S. Kim, B. Zhu, Design principle and assessing the correlations in Sb-doped Ba$_{0.5}$Sr$_{0.5}$FeO$_{3-\delta}$ perovskite oxide for enhanced oxygen reduction catalytic performance, J. Catal. 395 (2021) 168–177, https://doi.org/10.1016/j.jcat.2020.12.005.

[63] V. Cascos, L. Troncoso, J.A. Alonso, New families of M^{n+}-doped SrCo$_{1-x}$M$_x$O$_{3-\delta}$ perovskites performing as cathodes in solid-oxide fuel cells, Int. J. Hydrogen Energy 40 (2015) 11333–11341, https://doi.org/10.1016/j.ijhydene.2015.03.134.

[64] Y. Shen, F. Wang, X. Ma, T. He, $SrCo_{1-y}Ti_yO_{3-\delta}$ as potential cathode materials for intermediate-temperature solid oxide fuel cells, J. Power Sources 196 (2011) 7420–7425, https://doi.org/10.1016/j.jpowsour.2011.04.025.

[65] J.A. Dean, Lange's Handbook of Chemistry, fifteenth ed., McGraw-Hill, Inc, 1999. ISBN: 0-07-016384-7.

[66] A.A. Markov, I.A. Leonidov, M.V. Patrakeev, V.L. Kozhevnikov, O.A. Savinskaya, U.V. Ancharova, A.P. Nemudry, Structural stability and electrical transport in $SrFe_{1-x}Mo_xO_{3-\delta}$, Solid State Ionics 179 (2008) 1050–1053, https://doi.org/10.1016/j.ssi.2008.01.026.

[67] R. Wang, F. Jin, L. Ta, T. He, $SrCo_{1-x}Mo_xO_{3-\delta}$ perovskites as cathode materials for $LaGaO_3$-based intermediate-temperature solid oxide fuel cells, Solid State Ionics 288 (2016) 32–35, https://doi.org/10.1016/j.ssi.2015.11.030.

[68] F. Wang, Q. Zhou, T. He, G. Li, H. Ding, Novel $SrCo_{1-y}Nb_yO_{3-\delta}$ cathodes for intermediate-temperature solid oxide fuel cells, J. Power Sources 195 (2010) 3772–3778, https://doi.org/10.1016/j.jpowsour.2009.12.081.

[69] Y. Li, Y.N. Kim, J. Cheng, J.A. Alonso, Z. Hu, Y.-Y. Chin, T. Takami, M.T. Fernández-Díaz, H.-J. Lin, C.-T. Chen, L.H. Tjeng, A. Manthiram, J.B. Goodenough, Oxygen-Deficient perovskite $Sr_{0.7}Y_{0.3}CoO_{2.65-\delta}$ as a cathode for intermediate-temperature solid oxide fuel cells, Chem. Mater. 23 (2011) 5037–5044, https://doi.org/10.1021/cm202542q.

[70] L. Dos Santos-Gómez, J.M. Porras-Vázquez, E.R. Losilla, F. Martín, J.R. Ramos-Barrado, D. Marrero-López, Stability and performance of $La_{0.6}Sr_{0.4}Co_{0.2}Fe_{0.8}O_{3-\delta}$ nanostructured cathodes with $Ce_{0.8}Gd_{0.2}O_{1.9}$ surface coating, J. Power Sources 347 (2017) 178–185, https://doi.org/10.1016/j.jpowsour.2017.02.045.

[71] S. Mulmi, V. Thangadurai, A perovskite-type $Nd_{0.75}Sr_{0.25}Co_{0.8}Fe_{0.2}O_{3-\delta}$ cathode for advanced solid oxide fuel cells, Chem. Commun. 55 (2019) 3713, https://doi.org/10.1039/C9CC01054H.

[72] R. Küngas, A.S. Yu, J. Levine, J.M. Vohs, R.J. Gorte, An investigation of oxygen reduction kinetics in LSF electrodes, J. Electrochem. Soc. 160 (2013) F205–F211, https://doi.org/10.1149/2.011303jes.

[73] J. Fleig, Solid oxide fuel cell cathodes: polarization mechanisms and modeling of the electrochemical performance, Annu. Rev. Mater. Res. 33 (2003) 361–382, https://doi.org/10.1146/annurev.matsci.33.022802.093258.

[74] N.H. Perry, Roles of bulk and surface chemistry in the oxygen exchange kinetics and related properties of mixed conducting perovskite oxide electrodes, Materials 9 (2016) 858, https://doi.org/10.3390/ma9100858.

[75] R. Merkle, J. Maier, H.J.M. Bouwmeester, A linear free energy relationship for gas-solid interactions: correlation between surface rate constant and diffusion coefficient of oxygen tracer exchange for electron-rich perovskites, Angew. Chem. Int. Ed. 43 (2004) 5069–5073, https://doi.org/10.1002/anie.200460081.

[76] W. Jung, H.L. Tuller, A new model describing solid oxide fuel cell cathode kinetics: model thin film $SrTi_{1-x}Fe_xO_{3-\delta}$ mixed conducting oxides-a case study, Adv. Energy Mater. 1 (2011) 1184–1191, https://doi.org/10.1002/aenm.201100164.

[77] Q. Sun, L. Sun, Y. Dou, Q. Li, N. Li, L. Huo, H. Zhao, Insights into the oxygen reduction reaction on Cu-doped $SrFeO_{3-\delta}$ cathode for solid oxide fuel cells, J. Power Sources 497 (2021), 229877, https://doi.org/10.1016/j.jpowsour.2021.229877.

[78] A. Barbucci, P. Carpanese, G. Cerisola, M. Viviani, Electrochemical investigation of mixed ionic/electronic cathodes for SOFCs, Solid State Ionics 176 (2005) 1753–1758, https://doi.org/10.1016/j.ssi.2005.04.027.

[79] J. Zamudio-García, J.M. Porras-Vázquez, E.R. Losilla, D. Marrero-López, $LaCrO_3-CeO_2$-Based nanocomposite electrodes for efficient symmetrical solid oxide fuel cells, ACS Appl. Energy Mater. 5 (2022) 4536–4546, https://doi.org/10.1021/acsaem.1c04116.

[80] H. Cai, L. Zhang, J. Xu, J. Huang, X.L. Wei, Z. Song, W. Long, Cobalt–free $La_{0.5}Sr_{0.5}Fe_{0.9}Mo_{0.1}O_{3-\delta}$ electrode for symmetrical SOFC running on H_2 and CO fuels, Electrochim, Acta 320 (2019), 134642, https://doi.org/10.1016/j.electacta.2019.134642.

[81] L. dos Santos-Gómez, J. Hurtado, J.M. Porras-Vázquez, E.R. Losilla, D. Marrero-López, Durability and performance of CGO barriers and LSCF cathode deposited by spray-pyrolysis, J. Eur. Ceram. Soc. 38 (2018) 3518–3526, https://doi.org/10.1016/j.jeurceramsoc.2018.03.024.

[82] V. Zapata-Ramírez, L. dos Santos-Gómez, G.C. Mather, D. Marrero-López, D. Pérez-Coll, Enhanced intermediate-temperature electrochemical performance of air electrodes for solid oxide cells with spray-pyrolyzed active layers, ACS Appl. Mater. Interfaces 12 (2020) 10571–10578, https://doi.org/10.1021/acsami.9b22966.